Click Here for Full Article

Pore space percolation in sea ice single crystals

D. J. Pringle,[1,2] J. E. Miner,[2] H. Eicken,[2] and K. M. Golden[3]

[1] We have imaged sea ice single crystals with X-ray computed tomography, and characterized the thermal evolution of the pore space with percolation theory. Between $-18°C$ and $-3°C$ the porosity ranged from 2 to 12% and we found arrays of near-parallel intracrystalline brine layers whose connectivity and complex morphology varied with temperature. We have computed key porosity-dependent functions of classical percolation theory directly from the thermally driven pore space evolution of an individual sample. This analysis is novel for a natural material and provides the first direct demonstration of a connectivity threshold in the brine microstructure of sea ice. In previous works this critical behavior has been inferred indirectly from bulk property measurements in polycrystalline samples. From a finite-size scaling analysis we find a vertical critical porosity $p_{c,v} = 4.6 \pm 0.7\%$. We find lateral anisotropy with $p_{c,pll} = 9 \pm 2\%$ parallel to the layers and $p_{c,perp} = 14 \pm 4\%$ perpendicular to them. Lateral connectivity is established at higher brine volumes by the formation of thin necks between the brine layers. We relate these results to measured anisotropy in the bulk dc conductivity and fluid permeability using a dual porosity conceptual model. Our results shed new light on the complex microstructure of sea ice, highlighting single crystal anisotropy and a step toward a realistic transport property model for sea ice based on percolation theory. We present full experimental details of our imaging and segmentation methodology based on a phase relation formulation more widely applicable to ice-solute systems.

1. Introduction

[2] Sea ice is a dynamic porous medium due to the presence of brine inclusions whose volume fraction depends on temperature and bulk salinity. Brine is mostly incorporated during growth as intracrystalline layers and at grain boundaries [Weeks and Ackley, 1986; Eicken, 2003]. Inclusions shrink with cooling as brine salinity must increase to maintain thermohaline equilibrium with the surrounding ice, and vice versa for warming. Brine porosity can exceed 70% at the ice-ocean interface [Notz and Worster, 2008] and approach zero in cold, desalinated multiyear ice [Weeks and Ackley, 1986; Eicken, 2003]. Comparatively little is known, however, about associated changes in inclusion morphology and pore space connectivity. The present work is motivated by the dependence of sea ice properties on inclusion morphology and connectivity, and to gain insight into the processes governing pore space thermal evolution necessary to develop realistic predictive models of sea ice microstructure. Such questions are important since the microstructure controls bulk properties underpinning the large–scale behavior of sea ice, its role in earth's climate system, and as an important habitat for algal and bacterial communities [Thomas and Dieckmann, 2003].

[3] Bulk properties of sea ice are sensitive to the anisotropy, number density, connectedness, and temporal evolution of individual inclusions and secondary brine channel networks, each over a range of length scales. These properties and processes include remote sensing signatures [Hallikainen and Winebrenner, 1992; Golden et al., 1998b, 1998c], optical properties [Light et al., 2003], colonization of sea ice by microorganisms [Krembs et al., 2000] and pollutant transport [Pfirman et al., 1995]. Of special note is the fluid permeability which controls fluid flow in sea ice, affecting ice albedo through melt pond development [Eicken et al., 2004], nutrient delivery to microorganisms [Krembs et al., 2000] and salinity profile evolution [Cox and Weeks, 1975; Weeks and Ackley, 1986; Wettlaufer et al., 2000; Vancoppenolle et al., 2007].

[4] The widely held rule of thumb is that bulk sea ice is essentially impermeable for brine volume fractions below 5%, above which permeability increases rapidly [Cox and Weeks, 1975; Freitag, 1999; Freitag and Eicken, 2003; Eicken et al., 2004; Petrich et al., 2006]. This bulk behavior has been interpreted in terms of percolation theory [Golden et al., 1998a, 2007; Zhu et al., 2006]. Golden et al. [1998a] equated sea ice brine volume fraction with porosity and used an excluded volume model to explain the apparent

[1] Arctic Region Supercomputing Center, University of Alaska Fairbanks, Fairbanks, Alaska, USA.
[2] Geophysical Institute, University of Alaska Fairbanks, Fairbanks, Alaska, USA.
[3] Department of Mathematics, University of Utah, Salt Lake City, Utah, USA.

critical porosity for fluid permeability, $p_c \approx 5\%$. For a salinity of 5 ppt, typical for first year (FY) sea ice, this threshold corresponds to a critical temperature of approximately $-5°C$, dubbed the 'rule of fives' [*Golden et al.*, 1998a]. We extend the application of percolation theory, applying it here to the much smaller scale of brine inclusions within sea ice single crystals.

[5] In doing so, we address the lack of a detailed description of the thermal evolution of brine inclusions. This lack reflects several measurement challenges. Sample microstructure should not be disturbed during preparation and measurement, requiring careful thermal control. Inclusions show length scales from submillimeter brine layers to meter long channels, requiring scale-specific methods which necessarily have optimal resolution over only some range of these length scales. Imaging methods should be free of stereological and resolution artifacts [*Eicken et al.*, 2000; *Jerram and Higgins*, 2007].

[6] Average inclusion statistics have been derived in previous studies using thin section microscopy. *Perovich and Gow* [1996] reported brine inclusion number densities of 1.0 to 4.5 per mm^3. *Light et al.* [2003] resolved 24 pockets per mm^3, and a power law scaling of inclusion number density with length (highlighting the effect of imaging resolution). *Cole and Shapiro* [1998] described inclusion shapes that ranged from spherical to vertically elongated ellipsoids. Nevertheless, the limitations of thin section microscopy motivated the use of nondestructive tomography. Our work builds on the low-resolution X-ray tomography of *Kawamura* [1988] and later efforts by *Lange* [1988]. *Eicken et al.* [2000] used magnetic resonance imaging (MRI) to measure inclusion dimensions from 2D horizontal and vertical images of polycrystalline natural and tank-grown sea ice with a resolution of $0.2 \times 0.2 \times 1$ mm. They found an increase in inclusion length and elongation with warming, and good agreement with high-resolution thin section microscopy.

[7] In part due to the lack of pore evolution data, microstructural models of sea ice are highly simplified. The elongated brine channels and ice plate model of *Assur* [1960] remains the standard descriptive and engineering model for mechanical properties. An ellipsoidal inclusion model was later developed by *Tinga et al.* [1973] and applied by *Vant et al.* [1978] to the dielectric permittivity of sea ice, with parameter fitting (vertical aspect ratio, and inclination angle) from measurements in the range $0.1-40$ GHz. Effective medium models for thermal properties have used spherical brine and air inclusions [*Yen*, 1981; *Pringle et al.*, 2007]. In a step toward the development of a more realistic model of sea ice microstructure, we characterize here the anisotropic brine connectivity using percolation theory.

[8] Percolation theory addresses transitions in disordered multicomponent systems whose properties depend on component connectivity [e.g., *Stauffer and Aharony*, 1994; *Bunde and Havlin*, 1995; *Christensen and Moloney*, 2005]. Below a critical volume fraction p_c there are no percolating pathways spanning a sample, and properties near p_c show power law scaling related to $(p - p_c)$. In numerical lattice simulations, the volume fraction corresponds to the probability a site is occupied or a bond exists; in tomographic images such as ours, it corresponds to porosity. Percolation theory has been applied to a broad range of materials including rocks [*Broadbent and Hammersley*, 1957; *Bourbie and Zinszner*, 1985; *Fredrich et al.*, 2006], semiconductors [*Shklovskii and Efros*, 1984], thin films [*Davis et al.*, 1991], glacial ice [*Enting*, 1985], compressed powder aggregates [*Zhang et al.*, 1994], polycrystalline metals [*Chen and Schuh*, 2007], radar absorbing coatings [*Kusy and Turner*, 1971], and carbon nanotube composites [*Kyrylyuk and van der Schoot*, 2008].

[9] For these materials it is generally difficult to vary the volume fraction of the phase whose connectivity controls bulk properties. In rocks, for example, one must analyze different samples [*Bourbie and Zinszner*, 1985; *Fredrich et al.*, 2006]. In contrast, it is precisely the strong variation of sea ice porosity over a narrow temperature range that motivates our work, and our results offer insight into the dynamic mechanisms by which the pores space changes with temperature.

[10] Despite more than 50 years of applying percolation theory to disordered materials, key variables such as the infinite cluster density, percolation probability, and correlation length have only been computed as functions of the occupation probability primarily for idealized lattice models. A novelty of our work is that we have computed key percolation variables directly from the microstructure of a natural material, indeed from thermally driven variations in the sample.

[11] We have grown sea ice single crystals, the building blocks of polycrystalline sea ice, and imaged the thermal evolution of their complex pore space with X-ray computed tomography. We have characterized the structure by computing key functions of classical percolation theory and applying finite-size scaling methods. The scope of this article is to present full details of our X-ray CT imaging, discuss our revealing new images of intracrystalline brine inclusions, and to characterize the brine pore space using percolation theory. We compare our findings with simple traditional models of sea ice microstructure and discuss them in the context of sea ice fluid transport and electrical properties. Although beyond the scope of this paper, a future end point of this groundwork is the development of a realistic, percolation theory based model of sea ice microstructure from which material properties can be derived.

2. Methods
2.1. Single Crystal Sample Preparation

[12] Large single crystals of artificial sea ice were grown in a temperature-controlled cold room. Saline solutions were seeded with oriented single crystals of freshwater ice, following the method described by *Kawamura* [1986]. Blocks of fresh water ice up to 50 cm to a side and comprising decimeter-sized crystals, were extracted from a local gravel pit in Fairbanks, Alaska. Following determination of crystal-optical alignment with a universal stage, $1-2$ cm thick seed plates with horizontal c axes were cut. Ice was grown at $-8°C$ from solutions of 50:50% by weight InstantOcean™ artificial sea salt and X-ray contrast agent CsCl. Solutions were cooled close to their freezing point and the seed plate lowered onto their upper surface as a substrate for oriented ice growth. Universal stage analysis showed excellent crystallographic alignment in samples as large as $40 \times 20 \times 10$ cm.
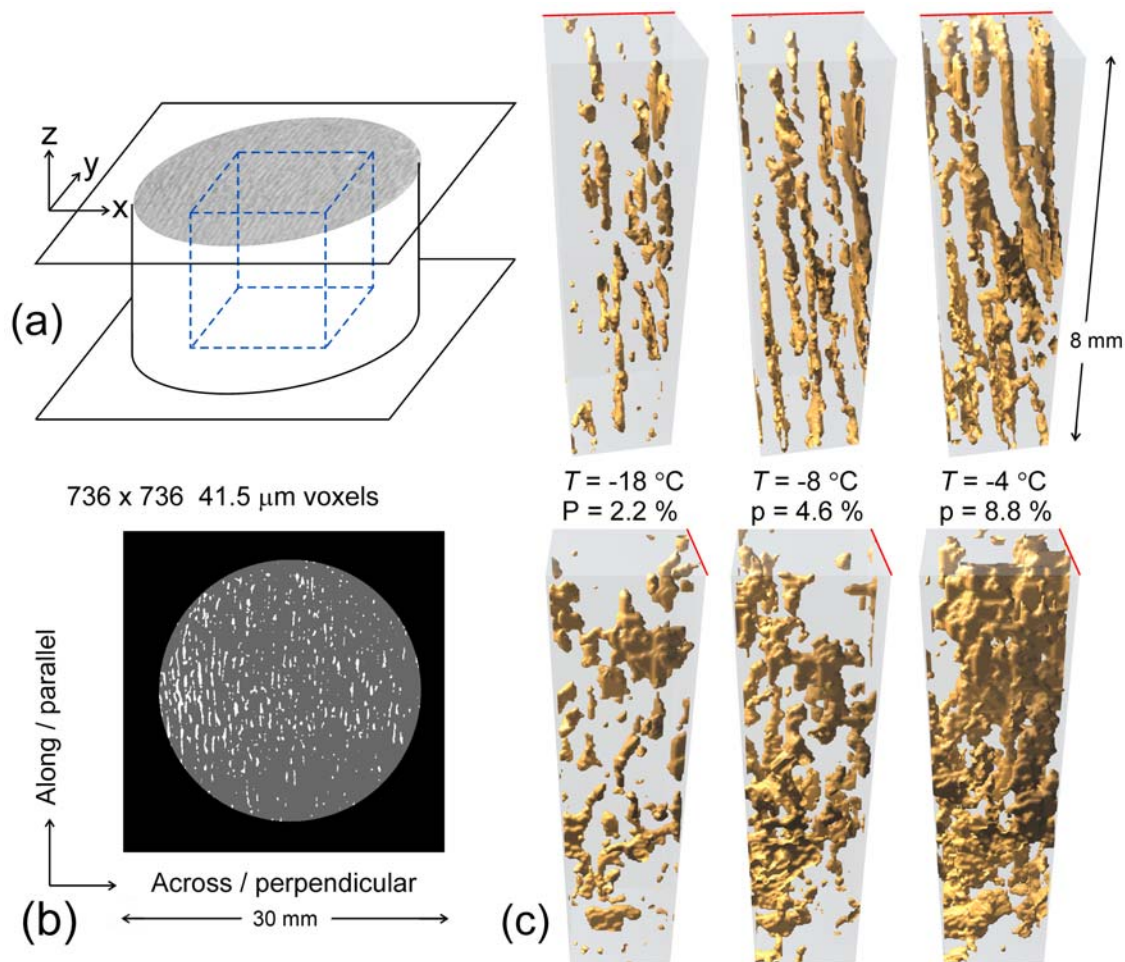
Figure 1. Imaging brine pore space with X-ray computed tomography. (a) Scanning outputs a stack of gray scale images. The blue dashed box is an example of a subvolume for which pore space connectivity was computed. (b) Gray scale images were segmented with each pixel designated as pore space (white) or ice (gray). (c) Images at different temperatures show the thermal evolution of the brine pore space. These volumes are nearly colocated and approximately $2 \times 2 \times 8$ mm. Figure 1c (top) shows the view approximately along the layers. The view across the layers is shown in Figure 1c (bottom) of the same volumes rotated about the vertical axis by 90°.

Tomography samples were prepared inside a cold room at −20°C, a sufficiently low temperature to inhibit brine drainage from the ice. Large single crystals were cut into several sections and turned down with a lathe until they fit tightly into 3 cm diameter, 3 cm tall, low-density polyethylene (LDPE) cylindrical sample holders. Bulk salinity and density profiles were obtained from parallel samples with a YSI 30 salinometer.

2.2. X-Ray Computed Tomography

[13]   X-ray measurements were performed with a Skyscan 1074 fan beam X-ray source micro-CT scanner, in a temperature-controlled subchamber of the cold room in which the samples were grown and prepared. These measurements return a 3D image of X-ray absorption.

[14]   The LDPE cylindrical sample holders were mounted on a stage and rotated about the vertical axis, with an X-ray absorption image taken at each 1° step. Results are output as a stack of horizontal images as shown in Figure 1a. Each image was a 736×736 pixel, 8 bit bitmap of X-ray absorption with 'CT' numbers in the range 0−255. Pixels were 41.5×41.5 μm. Using the maximum available sample size gave an image thickness also of 41.5 μm, so our 3D pore space images are composed of cubic voxels 41.5 μm to a side.

[15]   Images were acquired with the highest available energy, 40 keV ($\lambda = 0.31$ Å) and current (1mA) to reduce acquisition time. Resolution was maximized with an exposure time of 670 ms and each acquisition averaged over 8 repeat frames to reduce noise from external sources. A sequence of measurements was performed at different temperatures on individual samples without removal from the sample holder housed inside the scanner. Samples were cooled to −25°C, and successive measurements made at −18°C, −15°C, −12°C, −8°C, −7°C, −6°C, −5°C, −4°C, and −3°C. Visualization and analysis of these measurements requires identification of the brine and ice phases, which we now discuss.

Table 1. Target and Segmented Porosities

Temperature (°C)	Target Porosity $p*$[a] (%)	Integer Threshold Segmentation[b]	
		p_L (%)	p_H (%)
−3	11.67 ± 0.63	10.60	12.52
−4	8.81 ± 0.48	8.17	9.60
−5	7.12 ± 0.38	6.53	7.68
−6	6.00 ± 0.32	5.68	6.65
−7	5.22 ± 0.28	4.61	5.37
−8	4.64 ± 0.25	4.02	4.84
−12	3.06 ± 0.16	2.71	3.26
−15	2.54 ± 0.14	2.36	2.85
−18	2.24 ± 0.12	1.85	2.25

[a]Target porosity for $S = 9.4 \pm 0.5$ ppt.
[b]Segmented porosities from threshold segmentation with integer threshold CT giving p_L (closest but not above $p*$) and CT + 1 giving p_H (closest, but not below $p*$). Final results were found by interpolation to $p*$.

2.3. Image Processing and Segmentation

[16] In a process known as segmentation, the gray scale X-ray absorption images were processed so that each voxel was designated as either ice, brine, or air. The porosity is the combined volume of air and brine voxels. We first applied a 3×3 median filter to each slice to reduce noise with minimal edge loss, averaged vertically over 3 slices, and applied radial detrending. Air volumes typically less than 0.1% were formed by occasional brine movement. We then identified a global CT threshold for air by fitting double Gaussian peaks to manually chosen subvolumes with ice and air inclusions, but no brine inclusions. To segment brine from ice we exploited the known phase relation for sea ice, adapted to the InstantOcean™-CsCl-H$_2$0 system. This was necessary because ice and brine have a density contrast of only 20%. Even at the relatively low energy of 40 keV, the contrast due to the addition of high-atomic-number Cs was useful, but insufficient to unambiguously segment ice and brine for our dynamic range. The phase behavior of sea ice allows calculation of brine volume fraction from temperature T, bulk salinity S, and density ρ. We adapted the equations of *Cox and Weeks* [1983] and *Leppäranta and Manninen* [1988] to the InstantOcean™-CsCl-H$_2$0 system using the freezing point depression for the combined system (see Appendix A).

[17] Brine was segmented from ice with global thresholding such that the volume fraction of brine (plus the small contribution from air) matched the target porosity calculated from T, S and ρ. An exact match is not possible with integer thresholding, so we found the integer thresholds CT and CT + 1 giving porosities immediately above and below the target porosity. We processed in parallel the segmented data sets with these porosities and calculated final results by interpolation to the target porosity (see Table 1). Constrained by the known freezing point depression for our samples, this interpolation improved the resolution of our segmentation beyond that possible for unguided thresholding.

[18] The structure of the brine pore space is seen in isosurface plots in Figure 1. Plots for −18°C, −8°C and −4°C, show the pore space evolution as porosity changes from 2.2 to 4.6 to 8.8%. To more clearly show the structure, these are nearly collocated $50 \times 50 \times 200$ voxel subvolumes (approximately $2 \times 2 \times 8$ mm).

[19] The upper images clearly show near-parallel layering, but overall we see a pore space much more complicated than suggested by simple models of parallel ice lamellae and parallel brine sheets or tubes [e.g., *Assur*, 1960]. The cause of the near-parallel arrangement is crystallographic [*Weeks and Ackley*, 1986]. In fact the alignment of the brine layers align with the crystallographic basal plane (perpendicular to the c axis) can be used in the field to determine c axis orientation on extracted cores.

[20] In our images, the thickness of ice lamellae between brine layers is typically in the range 200−500 μm. In comparison, we note microbial length scales in sea ice: bacteria are typically in the 1−5 μm size range, and diatoms in the 10−200 μm size range [*Krembs et al.*, 2000; *Junge et al.*, 2001]. Indeed, microorganisms in sea ice pores are constrained by the length scale or volume over which they can access nutrients and dissolved organic matter and by their ability to move through the interconnected pore space.

[21] These images in Figure 1c illustrate aspects of the critical behavior analyzed below. At $p = 2.2\%$ we see many disconnected inclusions, and there is no vertically percolating path. At $p = 8.8\%$, there are shunts, or 'necks', connecting the layers, and the pore space is well connected from top to bottom. At $p = 4.6\%$, very close to the vertical percolation threshold computed below, the layers are vertically elongated with only a few necks. Figure 1c (bottom) show a side on view of the layers, with images rotated by 90°. Again, we see connectivity increasing with porosity as the pore space changes from isolated inclusions to extended, near-parallel layers. The lateral connectivity appears higher along the layers (Figure 1c (bottom)) than across them (Figure 1c (top)). In fact $p = 8.8\%$ is close to the lateral connectivity threshold we find parallel to the layers, whereas the threshold across the layers is higher still.

2.4. Pore Space Analysis With Three-Dimensional Medial Axis

[22] For the connectivity analysis of our 3D tomographic images, we used the freely available 3DMA software package. 3DMA-Rock (Three-Dimensional Medial Axis) is a modular research code which has been previously applied to a variety of porous media for pore space characterization and single- and two-phase pore fluid displacement [e.g., *Lindquist*, 1999; *Prodanović et al.*, 2006]. The medial axis of a digitized object is a centrally located skeleton which preserves the original topology and geometry of the object [*Lindquist*, 1999]. We use 3DMA to compute pore space connectivity, using the 26 connected medial axis as a search path. Here '26 connected' means that adjacent voxels on the medial axis can connect at any of the 26 corners, edges or faces of a voxel.

[23] As a comment on nomenclature, porous media microstructure is generally described in terms of 'pores' connected by 'throats'. Throats are local restrictions in the pore space, and control drainage, whereas pores control imbibition [e.g., *Hunt*, 2005]. Previous characterization of sea ice microstructure has focused on the length and size of discrete 'brine inclusions', neglecting the role of throats within these inclusions.

2.5. Key Functions of Percolation Theory

[24] Our tomographic images of brine and ice voxels are similar to 3D site percolation lattices [e.g., *Stauffer and Aharony*, 1994; *Bunde and Havlin*, 1995; *Christensen and*
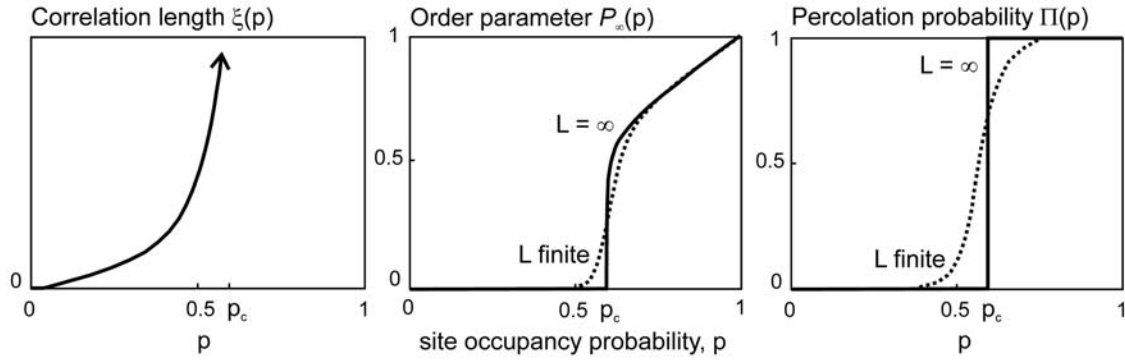
Figure 2. Key percolation functions shown for 2D site percolation, where site occupancy p is analogous to our sample porosity *p*, and here $p_c \approx 0.59$ [e.g., *Christensen and Moloney*, 2005]. The correlation length is shown only for $p < p_c$ relevant to our work [*Christensen and Moloney*, 2005]. Order parameter results from 2D site percolation theory [*Christensen and Moloney*, 2005]. See text for percolation probability definitions [*Stauffer and Aharony*, 1994].

Moloney, 2005], with sea ice porosity analogous to lattice site occupancy probability. Figure 2 illustrates the behavior of three percolation functions central to our work.

[25] The correlation function is the probability that two points separated by *r* are connected through the phase of interest, in our case, the pore space. When *r* is large (see next paragraph), the two-point correlation function behaves as

$$g(r) \sim \exp(-r/\xi),\qquad(1)$$

where ξ is the correlation length. In site percolation ξ is the mean distance between two sites on the same finite cluster, and is given by

$$\xi(p) \sim |p - p_c|^{-\nu},\qquad(2)$$

where ν is the correlation length critical exponent, which has a universal value depending only on the system dimension, and $\nu = 0.876$ in 3D [*Bunde and Havlin*, 1995]. We do not consider the correlation length above p_c as here it is defined for the matrix phase, in our case ice. The criterion above that '*r* is large' is that $r > \xi$, which is satisfied for our low porosity samples for which the correlation length is small, and we do observe exponential behavior.

[26] The order parameter $P_\infty(p)$ is also known as the 'infinite cluster density' in infinite samples. It is the probability that any randomly chosen position is on a percolating path. For $p < p_c$, $P_\infty(p) = 0$, and $P_\infty(p) = 1$ only at $p = 1$. See Figure 2. As *p* approaches p_c from above, $P_\infty(p)$ vanishes as

$$P_\infty(p) \sim (p - p_c)^{\beta}.\qquad(3)$$

Here β is also a universal exponent, with $\beta = 0.418$ in 3D [*Bunde and Havlin*, 1995].

[27] The percolation probability $\Pi(p)$ is the probability there exists a percolating path across a sample. For an infinite lattice, $\Pi(p)$ is a step function with $\Pi(p < p_c) = 0$ and $\Pi(p > p_c) = 1$. Figure 2 shows the behavior of these

quantities in infinite samples, for which they are defined, and for finite samples in which we are presently interested.

[28] 'Finite-size scaling' describes percolation behavior in finite systems at the percolation threshold $p = p_c$. At p_c the correlation length ξ diverges and is therefore always greater than the system size *L*. This leads to properties which are related to p_c showing power law scaling with *L* [e.g., *Stauffer and Aharony*, 1994; *Bunde and Havlin*, 1995; *Christensen and Moloney*, 2005]. We have used results of finite size scaling to compute intrinsic infinite sample thresholds from our finite size samples.

3. Computational Results and Analysis

[29] We have analyzed the connectivity of the pore space as a whole using 3DMA. Input was a series of X-ray tomography image stacks from a single-crystal sample processed as above and imaged between $-18°C$ and $-3°C$. We analyzed this sample over a 7.5 mm thickness with a constant salinity $S = 9.4 \pm 0.5$ ppt.

[30] Using 3DMA, we have calculated the vertical correlation length as a function of porosity and have used finite-size scaling to calculate anisotropic percolation thresholds. These measures were derived from the fractional connectivity *f* computed between two faces of cuboid volumes in our samples. Here *f* is the fraction of medial axis voxels on the start face which are connected via a percolating medial axis path to the opposite end face. The fractional connectivity is a measure of whether there is at least one spanning path from each start voxel, and is insensitive to the number and properties of these paths.

3.1. Correlation Length and Connectivity Depth Dependence

[31] We have derived the porosity dependence of the correlation length in the vertical direction from the depth dependence of the fractional connectivity. Using cuboid samples with horizontal extent 380 × 380 voxels, we computed the fractional connectivity over increasing depths, from the surface to a maximum depth of $z = 180$ voxels. From equation (1), we expect an exponential decay in *f(z)* when the correlation length is smaller than the sample
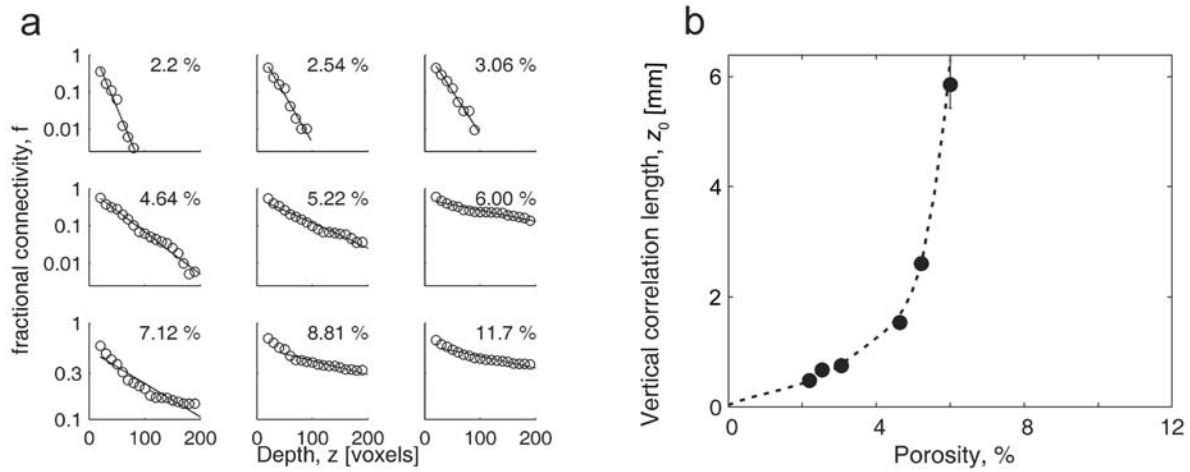
Figure 3. Vertical correlation length. (a) Log linear plot of fractional connectivity versus depth. Labels are sample porosity. Lines are fits of the form $f(z) = C \exp(-z/z_0)$. Logarithmic vertical scale is the same for each plot in a row; note change in scale in bottom plots. Horizontal scale is the same in all plots. Numbers omitted for clarity. (b) Penetration depth z_0 for $p \le 6.00\%$. The dashed line is a guide to the eye, showing divergence toward the sample depth 7.5 mm ($L = 180$ voxels).

depth, and Figure 3a shows that we see this at low porosities. The fitted lines are of the form: $f = C \exp(-z/z_0)$, where C is a constant and z_0 a penetration depth. At high porosities we do not expect exponential behavior because for $p > p_c$ the correlation length is related to the ice phase not the pore space. In fact we found power law behavior for $p > 7\%$ with good fits of the form $f = kz^\alpha$, where k is a constant.

[32] The fitted values of z_0 for $p < p_c$ correspond to a vertical correlation length ξ_V as in equation (1) for connections between two parallel planes. We will see that the connecting pathways are preferentially vertical, so that multiplying the fractional connectivity by the porosity approximates well the two-point correlation function in the vertical direction. This multiplication does not affect the fitted penetration depths z_0 in Figure 3a, only the prefactors C. Figure 3b shows the fitted z_0 values for $p \le 6\%$. In an infinite domain, ξ diverges as p increases toward p_c. It is bounded by the sample size in a finite system, and Figure 3b shows z_0 to be approaching the sample size $L = 180$ voxels (7.5 mm) for $p \approx 6\%$.

[33] Ultimately, we are interested in the intrinsic, scale-independent threshold p_c. In the absence of analytical results for $\xi(p)$ in finite systems, we cannot extrapolate to the intrinsic threshold. We have instead computed p_c with methods from finite scaling [*Christensen and Moloney*, 2005].

3.2. Percolation Thresholds From Finite-Size Scaling

[34] Finite-size scaling allows for the calculation of intrinsic thresholds from the variation of measured quantities as a function of sample size. Analytical finite-size scaling results have been developed from lattice simulations using variations in lattice size of many orders of magnitude [*Christensen and Moloney*, 2005]. We have applied these results to subvolumes of our samples at different temperatures, and computed the vertical percolation threshold with four methods. The weighted mean of these values gives $p_{c,v} = 4.6 \pm 0.7\%$.

[35] The range of length scales that we can analyze is limited by the finite resolution of our tomographic data, and is necessarily less than the order of magnitude variations used in lattice simulations, or indeed scaling law studies of fracture statistics in geological materials [e.g., *Odling*, 1997; *Bour et al.*, 2002]. Nevertheless, these methods provide potentially valuable insight into the anisotropic critical thresholds, and we proceed on the basis of the finite-scaling laws of percolation theory being size independent. The reduced range of length scales we have been able to analyze has required attention to uncertainties when calculating these thresholds. Ultimately, we find differences in the anisotropic thresholds which exceed the uncertainties in these values, see Table 2.

[36] We have computed the connectivity for ensembles of cubic subvolumes with side lengths $L = 50, 75, 100, 125, 150$ and 180 voxels (2.0, 3.1, 4.2, 5.2, 6.2, 7.5 mm). These volumes were positioned in a (pseudo-) random fashion [*Matsumoto and Nishimura*, 1998] and excluded sample boundaries (see Figure 1a). The number of subvolumes was scaled as $N_L \propto L^{-3}$ in order to hold constant the total volume sampled for each length scale. From each ensemble we computed the finite-size versions of the percolation probability Π and the order parameter P_∞.

Table 2. Summary of Intrinsic Thresholds Calculated With Finite Size Scaling

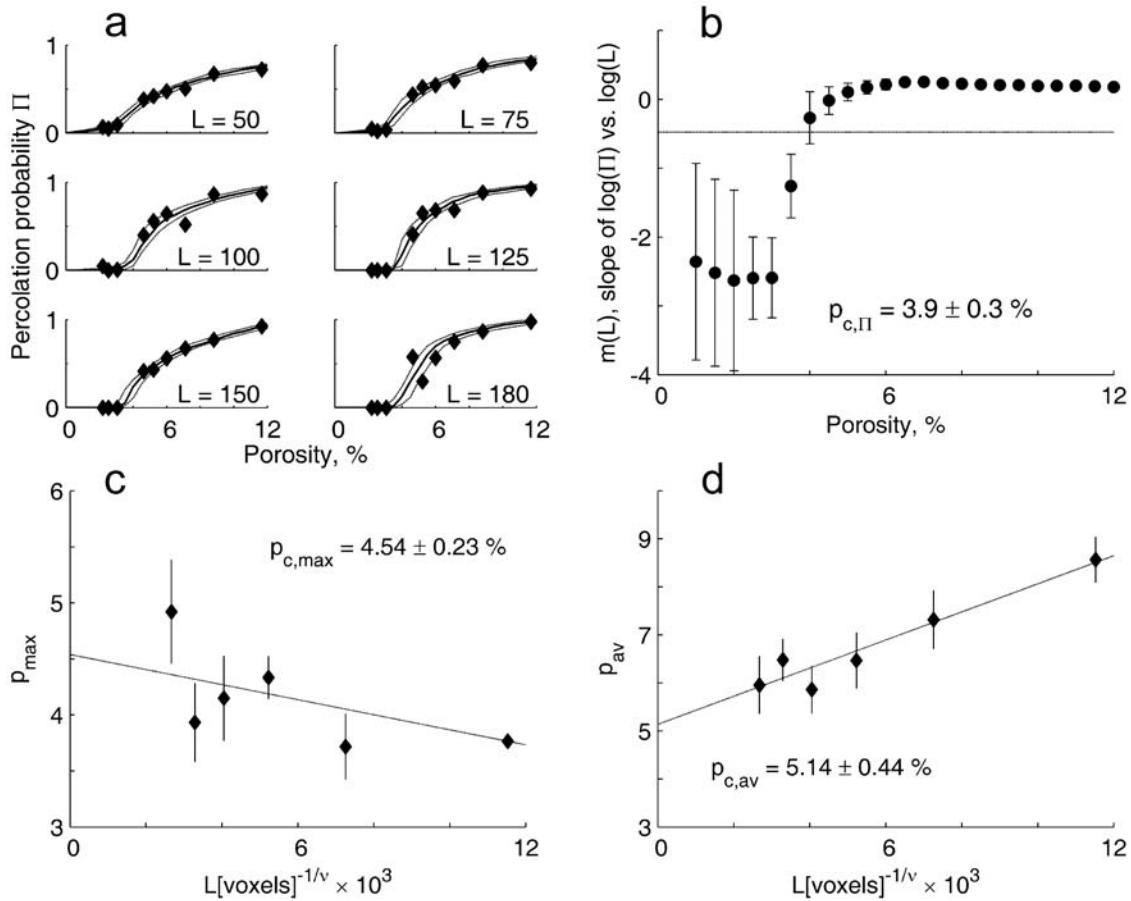| Threshold	Equation/Method	p_c (%)
Vertical $p_{c,v}$	$\Pi(p_c, L) \propto L^{-\beta/\nu}$	3.9 ± 0.3
Vertical $p_{c,v}$	$(p_{\max} - p_c) \propto L^{-1/\nu}$	4.54 ± 0.23
Vertical $p_{c,v}$	$(p_{av} - p_c) \propto L^{-1/\nu}$	5.14 ± 0.44
Vertical $p_{c,v}$	$P_\infty(p_c, L) \propto L^{-\beta/\nu}$	6.9 ± 0.7
Vertical $p_{c,v}$	Weighted mean	4.6 ± 0.7
Horizontal parallel to layers $p_{c,pll}$	$\Pi(p)$ mapping	9 ± 2
Horizontal perpendicular to layers $p_{c,perp}$	$\Pi(p)$ mapping	14 ± 4

Figure 4. Finite-size percolation probability $\Pi(p, L)$. (a) Points are computed values and lines smooth interpolations. Subplots have the same limits, omitted for clarity. (b) Calculation of p_c from power law scaling $\Pi(p_c, L) \propto L^{-\beta/\nu}$. The line is $m(L) = -\beta/\nu = -0.477$. Finite scaling of (c) p_{max} and (d) p_{av} with $L^{-1/\nu}$, where L is in units of voxels. Points and error bars are the mean and standard deviations derived from the curves in Figure 4a. Lines are weighted least square fits with intercepts giving $p_{c,max} = 4.54 \pm 0.23\%$ and $p_{c,av} = 5.14 \pm 0.44\%$.

[37] $\Pi(p, L)$ is the probability of a percolating pathway across a sample of porosity p and size L [*Christensen and Moloney*, 2005]. We compute $\Pi(p, L)$ as the fraction of subvolumes with one or more percolating paths in each ensemble [*Biswal et al.*, 1998]. For an infinite sample, $\Pi(p)$ is a step function with $\Pi(p < p_c) = 0$ and $\Pi(p > p_c) = 1$. This step widens as the sample size decreases. As seen in Figure 4a, the porosity range of our samples is wide enough to cover the full transition from $\Pi(p, L) = 0$ to 1 when $L = 180$ (7.5 mm), but not for $L < 180$.

[38] We have found three estimates of the vertical threshold $p_{c,v}$ from the finite-size scaling of $\Pi(p, L)$. To improve our porosity resolution we analyzed smooth curves fit to our data in Figure 4a, with the upper and lower curves used for uncertainty analysis. These curves are all smooth interpolations because although scaling results exist at p_c, there are no analytical results for the full curves.

[39] We first estimate p_c from the scaling of $\Pi(p, L)$ with respect to L. When $p = p_c$, this is given by

$$\Pi(p_c, L) \propto L^{-\beta/\nu}, \tag{4}$$

with β and ν as in section 2.5 [*Stauffer and Aharony*, 1994; *Christensen and Moloney*, 2005]. Equation (4) implies that at p_c a log-log plot of $\Pi(p, L)$ against L is linear with a gradient $m(L)$ given by

$$m(L) = \frac{d(\log \Pi)}{d(\log L)}\bigg|_{p_c} = -\beta/\nu. \tag{5}$$

Therefore p_c can be found as the porosity for which $m(L) = -\beta/\nu = -0.477$. Figure 4b shows $m(L)$ calculated from the smooth curves in Figure 4a. Interpolating between points adjacent to the target value $m(L) = -0.477$ gives $p_{c,\Pi} = 3.9 \pm 0.3\%$. Standard errors in $m(L)$ come from weighted linear least squares fits using uncertainties from the outer curves in Figure 4a [*Krystek and Anton*, 2007].

[40] We observe several percolation features in Figure 4b. For porosities both much smaller and much larger than $p_{c,\Pi}$ we find $m(L)$ approaching 0. We expect $m(L) = 0$ for both $p = 0$ and 1 because percolation cannot occur for any value of L at $p = 0$, and percolation occurs for all L at $p = 1$. For p between 0 and the transition region, $m(L)$ is negative because smaller samples admit an increasing chance of
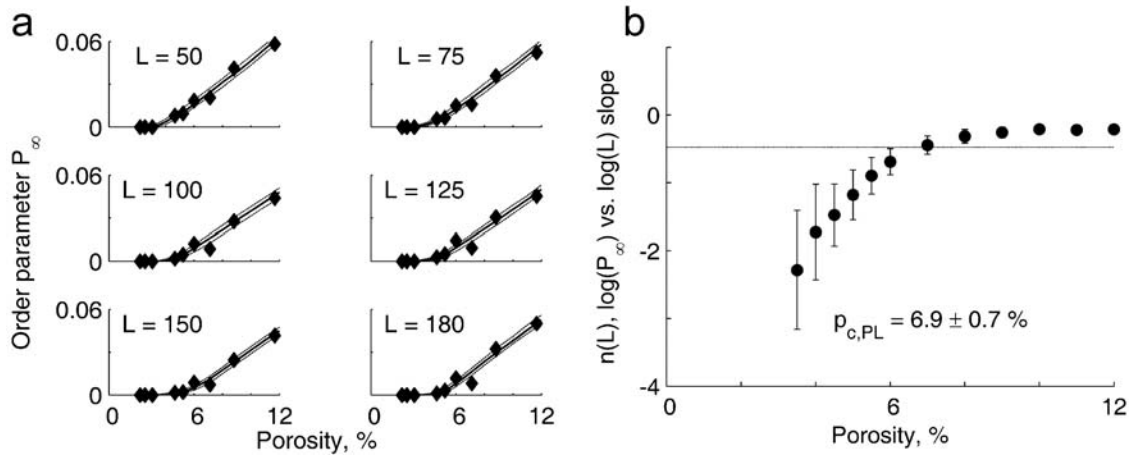
Figure 5. Order parameter $P_\infty(p, L)$ and derived value of p_c. (a) $P_\infty(p, L)$ points from ensemble computations where lines are interpolated fits. All plots have the same limits, omitted for clarity. (b) Calculation of p_c derived from the power law scaling of $P_\infty(p, L)$ with L at $p = p_c$. Line shows $n(L) = -\beta/\nu = -0.477$. Uncertainties are standard error in $n(L)$ from weighted linear fits. L is in units of voxels.

percolation below the infinite sample threshold. Similarly, between the transition region and $p = 1$, $m(L)$ is positive since smaller samples also admit an increasing chance of no percolation above p_c.

[41] We found two further estimates of p_c from the $\Pi(p, L)$ curves in Figure 4a. The point of inflection p_{max} of these curves converges to p_c as [Stauffer and Aharony, 1994]

$$(p_{max} - p_c) \propto L^{-1/\nu}. \qquad (6)$$

From the curves in Figure 4a, we have numerically calculated $d\Pi/dp$ and found $p_{max}(L)$ as the porosity with maximum $d\Pi/dp$. Figure 4c shows plots of p_{max} versus $L^{-1/\nu}$, where uncertainties give the range in p_{max} derived from the dashed curves in Figure 4a. As L increases, $L^{-1/\nu}$ decreases so the value of p_c for the infinite size limit is given by the vertical axis intercept. A weighted linear least squares fit gives an intercept of $p_{c,max} = 4.54 \pm 0.23\%$. The uncertainty here is the least squares estimate of the intercept standard error [Krystek and Anton, 2007].

[42] Similar scaling is displayed by p_{av}, the average porosity at which a percolating cluster appears for the first time. This is given by [Stauffer and Aharony, 1994]

$$p_{av} = \int_0^1 p\left(\frac{d\Pi}{dp}\right) dp. \qquad (7)$$

The special case of $\Pi(p, L)$ being symmetric is not met for our data, so p_{av} scales as for p_{max}: [Stauffer and Aharony, 1994]

$$(p_{av} - p_c) \propto L^{-1/\nu}. \qquad (8)$$

Values of p_{av} calculated with equation (7) are plotted against $L^{-1/\nu}$ in Figure 4d. A least squares fit here gives an intercept of $p_{c,av} = 5.14 \pm 0.44\%$. Uncertainties are as for p_{max} above.

[43] $P_\infty(p, L)$ is the finite-size order parameter. In our case, this is the probability that any voxel is connected

through the brine phase to both the top and bottom of the sample. Figure 5a shows ensemble average values for $P_\infty(p, L)$ found with a burn algorithm to compute the volume fraction of brine contained in the spanning paths.

[44] Figure 5a shows the resulting plots of $P_\infty(p, L)$ against porosity for each length scale. As in Figure 4a, the points are computed values, and the lines smooth interpolations used in our analysis. We resolve only a small portion of the P_∞ curves, which, as shown in Figure 2, reach $P_\infty = 1$ only at $p = 1$. We see an increase with L in the porosity at which P_∞ becomes nonzero. This is expected because with decreasing sample size, the appearance of the first percolating path becomes increasingly probable below p_c.

[45] We have calculated p_c from the scaling of $P_\infty(p, L)$ with L, which is the same as for $\Pi(p, L)$

$$P_\infty(p_c, L) \propto L^{-\beta/\nu}. \qquad (9)$$

[46] Figure 5b shows results from the same log-log scaling analysis applied above to $\Pi(p, L)$, now expressed in terms of $n(L)$:

$$n(L) = \left.\frac{d(\log P_\infty)}{d(\log L)}\right|_{p_c} = -\beta/\nu. \qquad (10)$$

[47] Interpolating between points adjacent to the target value $n(L) = -0.477$ gives $p_{c,PL} = 6.9 \pm 0.7\%$. Numerical simulations in fact suggest that this method may overestimate p_c. Christensen and Moloney [2005] show that the scaling of $P_\infty(p_c, L)$ for 2D site percolation obeys equation (10) only for L greater than about 100. For L between 10 and 100, their results suggest the power law exponent is about twice $-\beta/\nu$. Due to differences with 2D site percolation we don't necessarily expect this result to apply to our system. Nevertheless, revising our target scaling to $m(L) = -2\beta/\nu = -0.954$ gives $p_c = 5.3 \pm 0.7\%$, closer to the other estimates above.
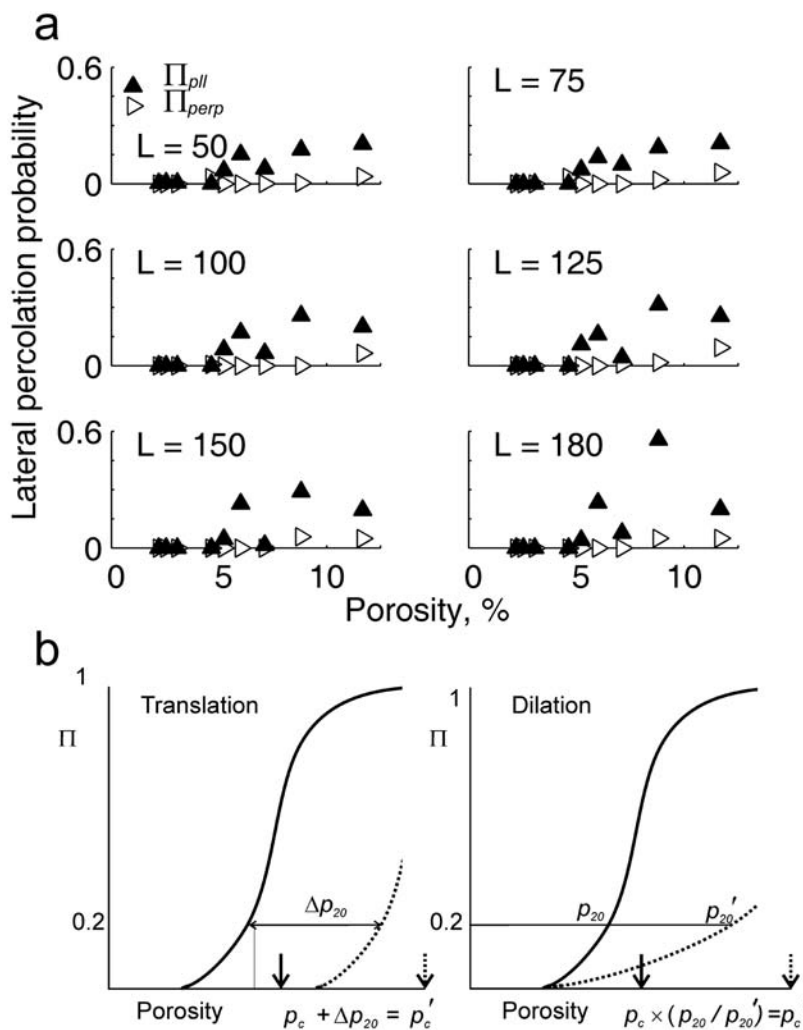
Figure 6. Horizontal percolation anisotropy. (a) Percolation probability Π_{pll} parallel to brine layers, and Π_{perp} perpendicular to brine layers. Plots have the same limits, omitted for clarity. (b) Simple translation and dilation scaling to estimate lateral thresholds p'_c from vertical p_c. Solid curves represent vertical $\Pi(p)$ and dashed curves represent lateral Π. The porosity for which $\Pi = 0.20$ in the vertical curves is p_{20} and for the lateral curves is p'_{20}. Scaling was done for p_{20} and p_5. L is in units of voxels.

[48] Finite-size widening of the transition means we do not observe the classic percolation result that the gradient dP_∞/dp diverges at p_c in an infinite sample. We are not aware of any scaling results for the widening of this transition for finite samples. Indeed numerical simulations with lattice dimensions of 5000 show the scaling predicted by equation (2) holds only exceptionally close to the critical porosity, i.e., $(p - p_c) \approx 10^{-2}$ [*Christensen and Moloney*, 2005].

[49] Our measurements have better resolved the percolation probability Π than the order parameter P_∞. From a percolation theory point of view, P_∞ is more fundamental. However, Π is in fact a more useful descriptor of pore space geometry, as it relates directly to the brine phase connectivity to which transport properties and processes are sensitive. In Table 2 we collate the vertical thresholds calculated above as well as their weighted mean. The lateral thresholds listed in Table 2 are described below.

3.3. Percolation Anisotropy

[50] We determined anisotropic horizontal thresholds with a similar analysis. The mean horizontal orientation of brine layers was computed at each temperature using the Quant3D code [*Ketcham and Ryan*, 2004; *Ketcham*, 2005], and the 3D image stacks rotated to align this direction with the y axis. To minimize the effect of image rotation on our analysis, we in fact rotated the raw output and then reapplied the preprocessing and segmentation. We then computed the 'parallel connectivity' along the brine layers, and the 'perpendicular connectivity' across the layers (see Figure 1b).

[51] We found a marked horizontal anisotropy in the percolation probability parallel to the layers (Π_{pll}) and perpendicular to them (Π_{perp}). In contrast to Π in the vertical, our porosity range does not span the critical transition regions for lateral connectivity and we resolve only partial curves for Π_{pll} and Π_{perp}. Results in Figure 6a suggest threshold behavior with a higher critical porosity

perpendicular to the the layers than across them, and with both higher than in the vertical, i.e., $\Pi_{perp} > \Pi_{pll} > \Pi_V$. The width of the transition width for Π_{pll} is also larger than in the vertical. These differences attest to the different geometry in the pore space connectivity as expected from the images in Figure 1c. We attribute the horizontal anisotropy to the role of the small necks between adjacent brine layers. Connectivity perpendicular to the layers is critically dependent on the presence of these connections. With increasing porosity, Π_{perp} becomes nonzero not until $p \approx 8\%$. Connectivity along the brine layers is enhanced by these necks, but is less dependent on them, and Π_{pll} is nonzero already by $p \approx 5\%$. This point is illustrated in Figure 1c in which all samples show a higher degree of connectedness along the brine layers (left to right in Figure 1c (bottom) than across Figure 1c (top)).

[52] We have not resolved enough of the Π_{pll} and Π_{perp} curves to repeat the finite scaling analysis applied above to Π. Instead, we found thresholds $p_{c,pll}$ and $p_{c,\ perp}$ using simple scaling arguments to map the partial curves of $\Pi_{perp}(p)$ and $\Pi_{pll}(p)$ to the $\Pi(p)$ curves in Figure 4a. Mapping by translation and dilation (Figure 6b) gave consistent results, with means $p_{c,pll} = 9 \pm 2\%$ and $p_{c,perp} = 14 \pm 4\%$. Uncertainties here reflect the scatter in Figure 6a in the small number of laterally percolating paths as well as the two scaling approaches. In the case of $L = 150$ and 180 (6.2 and 7.5 mm) this is compounded by the increasing overlap between ensemble subvolumes.

[53] We have derived our threshold estimates from the porosity range spanned by imaging the same sample at increasing temperatures. Any nonmonotonic connectivity variations are therefore nonphysical. Our connectivity analysis is dependent on the resolution (or not) of narrow throats. As in all porous media analysis of tomographic images, we are ultimately limited by voxel resolution and segmentation accuracy [*Fredrich et al.*, 2006; *Jerram and Higgins*, 2007]. However, by analyzing the smooth interpolated curves fit to our computed values of Π and P_∞, we are here able to smooth over variations caused by nonsystematic processing artifacts.

4. Discussion

[54] Our results on anisotropic single crystal percolation are a starting point from which to develop a percolation-based model of sea ice microstructure. While that development is beyond the scope of this paper, we discuss our results in the context of existing models and sea ice properties which are sensitive to brine connectivity.

[55] The classic model of *Assur* [1960] was developed to address the mechanical properties of sea ice. This model does not indicate when pore segregation occurs and does not allow for transitions in pore connectivity. Anisotropy is prescribed through a simple geometric model that does not capture the cross-layer connectivity we have addressed.

[56] With regard to ice mechanics, a potential link from our results is through the fracturing process. *Schulson* [1999] relates failure to the coalescence of preexisting cracks and flaws, i.e., brine layers at the microscopic scale [*Cole and Shapiro*, 1998]. Hence connectivity of oriented layers as studied here may be linked to failure of sea ice in compression or tension.

4.1. Connection With Bulk Sea Ice Properties

[57] Our results provide insight into measurements of the bulk electrical and hydraulic properties of sea ice. Our single crystal vertical threshold $p_c = 4.6 \pm 0.7\%$ is only slightly smaller than the bulk permeability threshold $p_c = 5.4\%$ found by *Petrich et al.* [2006] in a reanalysis of the original data from which *Cox and Weeks* [1975] reported $p_c = 5\%$. Fluid permeabilities 10–100 times larger in the vertical than the horizontal have been reported, with up to almost an order of magnitude anisotropy in the horizontal components [*Freitag*, 1999]. In light of our results, we explain the latter by the limited connectivity provided by necks between parallel brine layers. While such lateral connections have been observed anecdotally in sea ice thin sections [*Cole et al.*, 2002], it is not clear what controls their formation and growth.

[58] Recent cross borehole dc resistivity tomography in landfast FY ice revealed an increase in horizontal conductivity above a brine volume fraction $p \approx 8{-}10\%$ [*Ingham et al.*, 2008] and a vertical conductivity persisting to at least as low as $p \approx 2\%$ (M. Ingham, personal communication, 2008). At low porosity, the horizontal conductivity scaled via Archie's Law, with $\sigma_H = \sigma_b\, p^m$, where σ_b is the brine conductivity and $m = 2.88$ [*Ingham et al.*, 2008]. However, for $p > 8{-}10\%$ the conductivity increased more strongly than predicted by Archie's Law, indicating a transition in the brine connectivity.

[59] These bulk properties can be reconciled with our single crystal thresholds using a dual-porosity conceptual model for polycrystalline columnar ice. Such ice has vertically elongated single crystals described by our results, with larger brine features present on grain boundaries and through secondary channels, all of which are preferentially vertical [*Weeks and Ackley*, 1986; *Eicken*, 2003]. The fluid permeability is limited by flow path restrictions but the dc conductivity is not, and whereas the permeability is a measure of the connectivity of larger-diameter brine features, the conductivity is sensitive also to small scale connectivity. At sufficiently low porosity, the larger features disconnect from each other, but are weakly connected by intracrystalline brine layers. The probability of a connecting pathway, as measured by $\Pi(p, L)$, is nonzero for finite-sized samples even below the bulk threshold. Such micrometer-scale brine layer connections would give a finite conductivity but strongly limit the fluid permeability. This dual porosity model is anisotropic through both the single crystal anisotropy we have measured, and the preferential vertical orientation and connectivity of larger brine features indicated by the permeability anisotropy. Therefore, just as the horizontal connectivity in single crystal samples is limited by necks between layers, the horizontal conductivity over scales of tens of centimeters is limited by single crystal connections between larger brine drainage features.

4.2. Extension and Future Work

[60] To pursue these connections further, it would be useful to apply the methods developed in this work to make similar X-ray CT measurements to assess differences due to variations in growth rate and therefore mean interlamellar spacing [e.g., *Nakawo and Sinha*, 1984]. Furthermore, analysis of polycrystalline samples might enable separation of connectivity contributions from intracrystalline inclu-

sions and brine along grain boundaries, enabling quantitative development of a dual-porosity sea ice microstructure model. Measurements over repeat temperature cycling of carefully collocated samples would provide direct insight into the mechanisms driving thermal evolution of individual pores and throats [e.g., *Eicken et al.*, 2000; *Light et al.*, 2003]. Cycled measurements might also provide insight on hysteretic effects observed in dielectric measurements on single crystals [*Pringle et al.*, 2009].

[61] A resolution improvement of an order of magnitude or more may be achieved with synchrotron measurements, which would enable further porous medium analysis of pore and throat size distributions and critical pathway analysis. A key point in this regard will be to identify the pore space parameters most relevant to different sea ice process and transport studies, and to translate between these and parameters of interest in other porous media for which results and computational methods already exist. Many of these methods are mature in the study of other porous media [e.g., *Prodanović et al.*, 2006; *Fredrich et al.*, 2006; *Jerram and Higgins*, 2007] making multidisciplinary work attractive for further advances to understand sea ice microstructure. The 3D structures returned by high-resolution tomography may be used as domains for lattice Boltzmann modeling to compute permeability and study oil-water-ice interaction. Similar approaches have been applied to firn [*Freitag et al.*, 2002] and sandstones [e.g., *Fredrich et al.*, 2006]. Likewise, the microstructure may also be used as a domain for heat transfer and thermal evolution calculations, as applied to snow by *Kaempfer et al.* [2005].

4.3. Broader Implications for Frozen and Granular Materials

[62] Low-temperature connectivity and its associated length scales are of great importance for the role of sea ice and other impurity-laden ice bodies like permafrost as microbial habitats. The percolation probability curves in Figure 4a indicate that even at low porosities (corresponding to temperatures well below $-10°C$), significant fluid exchange may be sustained at length scales relevant for microbial processes in cold environments [*Deming and Eicken*, 2007]. The results presented here provide the first quantitative evidence of potential microstructural constraints on biological activity and genetic segregation in frozen materials. Moreover, the finite-size scaling analysis yields information on the temperature dependence of the length scales governing transport of nutrients and biogenic particulates in frozen media such as sea ice.

[63] Sea ice may serve as a high-homologous temperature analog in the study of a range of other materials in the solar system. The present findings shed light on a system that exhibits microstructural controls on porous fluid transport hypothesized for mantle and crustal materials [*Wark et al.*, 2003; *Roberts et al.*, 2007]. Melt percolation is a debated mechanism for planetary core formation, support for which has come from recent synchrotron imaging of synthetic olivine-iron-sulfide partial melt samples used for permeability computations with lattice Boltzmann modeling [*Roberts et al.*, 2007].

[64] The microstructural controls on pore space morphology within the brine layers evident in Figure 1 remain to be explored in more depth. The data do demonstrate, however,

that for ordered arrays of intracrystalline inclusions common in a range of artificial and geomaterials, anisotropy can account for as much as a factor three difference in the magnitude of the critical porosity. Due to its differential impact on electric and fluid transport properties, this anisotropy in p_c may be relevant as both a diagnostic of microstructural evolution and a controlling factor in transport through anisotropic media.

5. Conclusions

[65] We have presented X-ray computed tomography imaging of sea ice single crystals and a percolation theory analysis of the pore space connectivity. We have analyzed connectivity at $\sim100-1000$ μm length scales, relevant to nutrient delivery and physical processes. Pore space images illustrate arrays of vertically elongated near-parallel layers and occasional necks between them which underlie the percolation anisotropy. We have computed functions of geometric percolation theory directly from the thermal evolution of the digitized pore space and estimated anisotropic percolation thresholds. In view of previous measurements of sea ice transport properties from which threshold behavior has been inferred [e.g. *Golden et al.*, 1998a, 2007; *Petrich et al.*, 2006], these results are the first demonstration of connectivity thresholds computed directly from the microstructure of sea ice. We find a vertical percolation threshold of $4.6 \pm 0.7\%$ which is somewhat less than the current best estimate of 5.4% for the bulk threshold derived from transport measurements [*Petrich et al.*, 2006]. This difference is consistent with the expectation of bulk percolation in polycrystalline samples being sensitive to pathways along grain boundaries and flaws. Our finding of anisotropic percolation thresholds offers a basis to understand observations of anisotropy in bulk transport properties. Key to optimizing our measurement resolution and image segmentation were the use of an X-ray contrast agent and the derivation of (more widely applicable) equations for the phase behavior of freezing ice-solute mixtures.

[66] While we only consider columnar sea ice crystals, our work goes beyond previous microstructural approaches [*Assur*, 1960; *Vant et al.*, 1978; *Golden et al.*, 1998a] which were not able, or only marginally able, to capture several key aspects of sea ice transport properties and their temperature dependence. Sea ice single crystals are the fundamental building blocks of bulk polycrystalline sea ice. One approach to relating our singe crystal results to bulk sea ice properties is through the development of a porous medium dual porosity model of sea ice in which the matrix is characterized by anisotropic porosity thresholds. The development of such a model would require careful comparison with other microstructural characterization as well as measurements of bulk properties which depend on brine connectivity at both the intracrystalline scale and along grain boundaries; it is beyond the scope of this paper.

[67] Sea ice has a dynamic pore structure ranging over wide length scales. The porosity is easily controlled by varying temperature, making sea ice not only a fascinating porous medium in its own right but also providing an analog for other frozen and granular materials. Factors motivating further improvements in understanding sea ice microstructure include its climatic, environmental and biological

interactions. Based on the successful application of percolation theory here at the intracrystalline scale, and previously at the bulk scale [*Golden et al.*, 1998a, 2007], we conclude that percolation theory holds promise as a multi-scale framework to develop a realistic, predictive model of sea ice transport properties.

Appendix A: Freezing Point Depression of Mixed InstantOcean™-CsCl-H₂0 Solution

[68] We derive the freezing point depression for an aqueous solution mixture of InstantOcean™ and CsCl. The eutectic temperature T_E of CsCl(aq) is $-23.7°C$ [*Dubois et al.*, 1993; *Monnin and Dubois*, 1999], very close to that of hydrohalite (NaCl ·2H₂0) in seawater $T_E = -22.7°C$ [*Eicken*, 2003]. We limit ourselves to temperatures above these, and modify the approach of *Cox and Weeks* [1983] and *Leppäranta and Manninen* [1988], both of which use the following functional forms to find the brine volume fraction, v_b:

$$v_b = (1 - v_a) \frac{\rho_i S}{F_1(T) - \rho_i S F_2(T)}, \tag{A1a}$$

$$F_1(T) = \rho_b S_b (1 + k), \tag{A1b}$$

$$F_2(T) = \left((1 + C)(\rho_b / \rho_i) - C(\rho_b / \rho_p) - 1 \right). \tag{A1c}$$

Here i, a, b, p denote ice, air, brine and precipitates, respectively. S is bulk sea ice salinity and S_b is brine inclusion salinity. Two temperature-dependent precipitation coefficients are: $k = m_{s,p}/m_{s,b}$, the ratio of salt mass in precipitates to salt mass in brine, and $C = m_{s,p}/m_b$, the ratio of precipitate mass to brine mass [*Cox and Weeks*, 1983]. For these, we scale the values of *Cox and Weeks* [1983] for no CsCl precipitation.

[69] To apply equation (A1), we need the inverse freezing point depression relationship $S_b(T)$ for an aqueous mixture of InstantOcean™ and CsCl. We derive this using the weighted ionic strength approach of *Padwardhan and Kumar* [1986a, 1986b]. The ionic strength μ of a solute j is given by the sum over ions i

$$\mu_j = \frac{1}{2} \sum_i m_i z_i^2, \tag{A2}$$

where m_i is ionic molality (mols/liter) and z_i the integer (elementary) ionic charge. The freezing point depression T_θ of a mixture of such solutions is then given by [*Padwardhan and Kumar*, 1986a, 1986b]

$$T_\theta = \sum_j \frac{\mu_J}{\mu_T} T_{\theta,J}(\mu_T). \tag{A3}$$

Here $J = 1$ for InstantOcean™, J = 2 for CsCl, and $T_{\theta,J}(\mu_T)$ is the freezing point depression of each solution if it had the total ionic strength of the combined solution. Ionic strength can be converted to salinity using the composition and ionic

masses in InstantOcean™ and CsCl (aq). The conversion factors are

$$\mu_{IO}[\text{molal e}^2] = 0.020028\, S_{IO}[\text{ppt}], \tag{A4a}$$

$$\mu_{CsCl}[\text{molal e}^2] = 0.00594\, S_{CsCl}[\text{ppt}]. \tag{A4b}$$

For InstantOcean™ we used the freezing point depression of standard seawater [*Cox and Weeks*, 1983] and for CsCl (aq) the result of *Dubois et al.* [1993]. These are fits to experimental data

$$T_{\theta,IO}[°C] = -0.5989\, S - 1.142 \times 10^{-3} S^2 - 5.409 \times 10^{-4}\, S^3, \tag{A5a}$$

$$T_{\theta,CsCl}[°C] = -0.2049\, S - 4.96 \times 10^{-4} S^2 - 7.42 \times 10^{-5}\, S^3. \tag{A5b}$$

We evaluated equation (A3) using (A4) and (A5) for a 50:50 combination by weight of InstantOcean™ and CsCl. Curves fit to the results give:

$$T_\theta[°C] = -0.0403\, S - 9.579 \times 10^{-6} S^2 - 2.31 \times 10^{-7} S^3, \tag{A6a}$$

$$S_b[\text{ppt}] = -25.965\, T - 0.7442\, T^2 - 0.0107\, T^3. \tag{A6b}$$

Both fits have $r^2 = 1.0$. Finally, equation (A6b) is used in equations (A1) to calculate the brine volume fraction for our samples. They are approximately 25% less than corresponding brine volumes for pure sea ice of the same salinity which is due to the larger mass of Cs^+ ions compared with common sea ice cations, Na^+, Mg^{2+} and K^+. Equations (A6) are specific to our 50:50% by weight mixture of InstantOcean™ and CsCl but this approach can be applied in general to similar mixtures.

References

Assur, A. (1960), Composition of sea ice and its tensile strength, *Rep. 44*, U.S. Army Cold Region Res. and Eng. Lab., Hanover, N. H.

Biswal, B., C. Manwart, and D. Hilfer (1998), Three dimensional local porosity analysis of porous media, *Physica A*, *255*, 221–241, doi:10.1016/S0378-4371(98)00111-3.

Bour, O., P. Davy, C. Darcel, and N. E. Odling (2002), A statistical scaling model for fracture network geometry, with validation on a multiscale mapping of a joint network (Hornelen Basin, Norway), *J. Geophys. Res.*, *107*(B6), 2113, doi:10.1029/2001JB000176.

Bourbie, T., and B. Zinszner (1985), Hydraulic and acoustic properties as a function of porosity in Fontainebleau sandstone, *J. Geophys. Res.*, *90*, 11,524–11,532, doi:10.1029/JB090iB13p11524.

Broadbent, S. R., and J. M. Hammersley (1957), Percolation processes. Part I: Crystals and mazes, *Proc. Cambridge Philos. Soc.*, *53*, 629–641, doi:10.1017/S0305004100032680.

Bunde, A., and S. Havlin (1995), Percolation I, in *Fractals and Disordered Systems*, edited by A. Bunde and S. Havlin, pp. 59–114, Springer, Berlin.

Chen, Y., and C. A. Schuh (2007), Percolation of diffusional creep: A new universality class, *Phys. Rev. Lett.*, *98*, 035701.1–035701.4, doi:10.1103/PhysRevLett.98.035701.

Christensen, K., and N. R. Moloney (2005), *Complexity and Criticality*, Imp. Coll. Press, London.

Cole, D. M., and L. H. Shapiro (1998), Observations of brine drainage networks and microstructure of first-year sea ice, *J. Geophys. Res.*, *103*(C10), 21,739–21,750, doi:10.1029/98JC01264.

Cole, D. M., H. Eicken, L. H. Shapiro, and K. Frey (2002), Some observations of high porosity layers and brine drainage features in first-year sea ice, paper presented at 16th International Symposium on Ice, Int. Assoc. for Hydro-Environ. Eng. and Res., Dunedin, New Zealand, 2–6 Dec.

Cox, G. F. N., and W. F. Weeks (1975), Brine drainage and initial salt entrapment in sodium chloride ice, *Res. Rep. 345*, Cold Regions Res. and Eng. Lab., Hanover, N. H.

Cox, G. F. N., and W. F. Weeks (1983), Equations for determining the gas and brine volumes in sea-ice samples, *J. Glaciol.*, *29*, 306–316.

Davis, C. A., D. R. McKenzie, and R. C. McPhedran (1991), Optical properties and microstructure of thin silver films, *Opt. Commun.*, *85*, 70–82, doi:10.1016/0030-4018(91)90054-H.

Deming, J. W., and H. Eicken (2007), Life in ice, in *Planets and Life: The Emerging Science of Astrobiology*, edited by J. Baross and W. Sullivan, pp. 292–312, Cambridge Univ. Press, Cambridge, U. K.

Dubois, M., J. J. Royer, A. Weisbrod, and A. Shtuka (1993), Reconstruction of low-temperature phase diagrams using a constrained least squares method: Application to the H_2O-CsCl system, *Eur. J. Mineral.*, *5*, 1145–1152.

Eicken, H. (2003), From the microscopic, to the macroscopic, to the regional scale: Growth, microstructure and properties of sea ice, in *Sea Ice: An Introduction to Its Physics, Chemistry, Biology and Geology*, edited by D. N. Thomas and G. S. Dieckmann, pp. 22–81, Blackwell, Oxford, U. K.

Eicken, H., C. Bock, R. Wittig, H. Miller, and H.-O. Poertner (2000), Nuclear magnetic resonance imaging of sea ice pore fluids: Methods and thermal evolution of pore microstructure, *Cold Reg. Sci. Technol.*, *31*, 207–225, doi:10.1016/S0165-232X(00)00016-1.

Eicken, H., T. C. Grenfell, D. K. Perovich, J. A. Richter-Menge, and K. Frey (2004), Hydraulic controls of summer Arctic pack ice albedo, *J. Geophys. Res.*, *109*, C08007, doi:10.1029/2003JC001989.

Enting, I. G. (1985), A lattice statistics model for the age distribution of air bubbles in polar ice, *Nature*, *315*, 654–655, doi:10.1038/315654a0.

Fredrich, J. T., A. A. DiGiovanni, and D. R. Noble (2006), Predicting macroscopic transport properties using microscopic image data, *J. Geophys. Res.*, *111*, B03201, doi:10.1029/2005JB003774.

Freitag, J. (1999), Untersuchungen zur hydrologie des Arktischen meereises: Konsequenzen für den kleinskaligen stofftransport, Ph.D. thesis, 150 pp., Bremen Univ., Bremen, Germany.

Freitag, J., and H. Eicken (2003), Melt water circulation and permeability of Arctic summer sea ice derived from hydrological field experiments, *J. Glaciol.*, *49*, 349–358, doi:10.3189/172756503781830601.

Freitag, J., U. Dobrindt, and S. Kipfstuhl (2002), A new method for predicting transport properties of polar firn with respect to gases on the pore space scale, *Ann. Glaciol.*, *35*, 538–544, doi:10.3189/172756402781816582.

Golden, K. M., S. F. Ackley, and V. I. Lytle (1998a), The percolation phase transition in sea ice, *Science*, *282*, 2238–2241, doi:10.1126/science.282.5397.2238.

Golden, K. M., M. Cheney, K. H. Ding, A. K. Fung, T. C. Grenfell, D. Isaacson, J. A. Kong, S. V. Nghiem, J. Sulvester, and D. P. Winebrenner (1998b), Forward electromagnetic scattering models for sea ice, *IEEE Trans. Geosci. Remote Sens.*, *36*, 1655–1674, doi:10.1109/36.718637.

Golden, K. M., et al. (1998c), Inverse electromagnetic scattering models for sea ice, *IEEE Trans. Geosci. Remote Sens.*, *36*, 1675–1704, doi:10.1109/36.718638.

Golden, K. M., H. Eicken, A. L. Heaton, J. Miner, D. J. Pringle, and J. Zhu (2007), Thermal evolution of permeability and microstructure in sea ice, *Geophys. Res. Lett.*, *34*, L16501, doi:10.1029/2007GL030447.

Hallikainen, M., and D. P. Winebrenner (1992), The physical basis for sea ice remote sensing, in *Microwave Remote Sensing of Sea Ice*, *Geophys. Monogr. Ser.*, vol. 68, edited by F. D. Carsey, pp. 29–46, AGU, Washington, D. C.

Hunt, A. G. (2005), *Percolation Theory for Flow in Porous Media (Lecture Notes in Physics 674)*, Springer, New York.

Ingham, M., D. J. Pringle, and H. Eicken (2008), Cross-borehole resistivity tomography of sea ice, *Cold Reg. Sci. Technol.*, *52*, 263–277, doi:10.1016/j.coldregions.2007.05.002.

Jerram, D. A., and M. D. Higgins (2007), 3D analysis of rock textures: Quantifying igneous microstrucutres, *Elements*, *3*(4), 239–245, doi:10.2113/gselements.3.4.239.

Junge, K., C. Krembs, J. Deming, A. Stierle, and H. Eicken (2001), A microscopic approach to investigate bacteria under in situ conditions in sea-ice samples, *Ann. Glaciol.*, *33*, 304–310.

Kaempfer, T. U., M. Schneebeli, and S. A. Sokratov (2005), A microstructural approach to model heat transfer in snow, *Geophys. Res. Lett.*, *32*, L21503, doi:10.1029/2005GL023873.

Kawamura, T. (1986), A method for growing large single crystals of sea ice, *J. Glaciol.*, *32*, 302–303.

Kawamura, T. (1988), Observations of the internal structure of sea ice by X ray computed tomography, *J. Geophys. Res.*, *93*(C3), 2343–2350, doi:10.1029/JC093iC03p02343.

Ketcham, R. A. (2005), Three-dimensional textural measurements using high-resolution X-ray computed tomography, *J. Struct. Geol.*, *27*, 1217–1228, doi:10.1016/j.jsg.2005.02.006.

Ketcham, R. A., and T. Ryan (2004), Quantification and visualization of anisotropy in trabecular bone, *J. Microsc.*, *213*, 158–171, doi:10.1111/j.1365-2818.2004.01277.x.

Krembs, C., R. Gradinger, and M. Spindler (2000), Implications of brine channel geometry and surface area for the interaction of sympagic organisms in Arctic sea ice, *J. Exp. Mar. Biol. Ecol.*, *243*, 55–80, doi:10.1016/S0022-0981(99)00111-2.

Krystek, M., and M. A. Anton (2007), A weighted total least-squares algorithm for fitting a straight line, *Meas. Sci. Technol.*, *18*, 3438–3442, doi:10.1088/0957-0233/18/11/025.

Kusy, R. P., and D. T. Turner (1971), Electrical resistivity of a polymeric insulator containing segregated metallic particles, *Nature*, *229*, 58–59.

Kyrylyuk, A. V., and P. van der Schoot (2008), Continuum percolation of carbon nanotubes in polymeric and colloidal media, *Proc. Natl. Acad. Sci. U. S. A.*, *105*, 8221–8226, doi:10.1073/pnas.0711449105.

Lange, M. A. (1988), Basic properties of Antarctic sea ice as revealed by textural analysis of ice cores, *Ann. Glaciol.*, *10*, 95–101.

Leppäranta, M., and T. Manninen (1988), The brine and gas content of sea ice with attention to low salinities and high temperatures, *Intern. Rep. 2*, Finn. Inst. of Mar. Res., Helsinki.

Light, B., G. A. Maykut, and T. C. Grenfell (2003), Effects of temperature on the microstructure of first-year Arctic sea ice, *J. Geophys. Res.*, *108*(C2), 3051, doi:10.1029/2001JC000887.

Lindquist, W. B. (1999), 3DMA general users manual, *Rep. SUNYSB-AMS-99–20*, State Univ. of N. Y. at Stony Brook, Stony Brook, N. Y.

Matsumoto, M., and T. Nishimura (1998), Mersenne twister: A 623-dimensionally equidistributed uniform pseudorandom number generator, *ACM Trans. Model. Comput. Simul.*, *8*(1), 3–30, doi:10.1145/272991.272995.

Monnin, C., and M. Dubois (1999), Thermodynamics of the CsCl-H_2O system at low temperatures, *Eur. J. Mineral.*, *11*(3), 477–482.

Nakawo, M., and N. K. Sinha (1984), A note on brine layer spacing of first-year sea ice, *Atmos. Ocean*, *22*(2), 193–206.

Notz, D., and M. G. Worster (2008), In situ measurements of the evolution of young sea ice, *J. Geophys. Res.*, *113*, C03001, doi:10.1029/2007JC004333.

Odling, N. E. (1997), Scaling and connectivity of joint systems in sandstones from western Norway, *J. Struct. Geol.*, *19*(10), 1257–1271, doi:10.1016/S0191-8141(97)00041-2.

Patwardhan, V. S., and A. Kumar (1986a), A unified approach for prediction of thermodynamic properties of aqueous mixed-electrolyte solutions, part 1: Vapor pressure and heat of vaporization, *AIChE J.*, *32*(9), 1419–1428, doi:10.1002/aic.690320903.

Patwardhan, V. S., and A. Kumar (1986b), A unified approach fro prediction of thermodynamic properties of aqueous mixed-electrolyte solutions, part 2: Volume, thermal, and other properties, *AIChE J.*, *32*(9), 1429–1438, doi:10.1002/aic.690320904.

Perovich, D. K., and A. J. Gow (1996), A quantitative description of sea ice inclusions, *J. Geophys. Res.*, *101*(C8), 18,327–18,343, doi:10.1029/96JC01688.

Petrich, C., P. J. Langhorne, and Z. F. Sun (2006), Modelling the interrelationships between permeability, effective porosity and total porosity in sea ice, *Cold Reg. Sci. Technol.*, *44*, 131–144, doi:10.1016/j.coldregions.2005.10.001.

Pfirman, S. L., H. Eicken, D. Bauch, and W. F. Weeks (1995), The potential transport of pollutants by Arctic sea ice, *Sci. Total Environ.*, *159*, 129–146, doi:10.1016/0048-9697(95)04174-Y.

Pringle, D., G. Dubuis, and H. Eicken (2009), Impedance measurements of the complex dielectric permittivity of sea ice at 50 MHz: Pore microstructure and potential for salinity monitoring, *J. Glaciol.*, *55*, 81–94, doi:10.3189/002214309788608903.

Pringle, D. J., H. Eicken, H. J. Trodahl, and L. G. E. Backstrom (2007), Thermal conductivity of landfast Antarctic and Arctic sea ice, *J. Geophys. Res.*, *112*, C04017, doi:10.1029/2006JC003641.

Prodanović, M., W. B. Lindquist, and R. S. Seright (2006), Porous structure and fluid partitioning in polyethylene cores from 3D X-ray microtomo-

graphic imaging, *J. Colloid Interface Sci.*, *298*, 282–297, doi:10.1016/j.jcis.2005.11.053.

Roberts, J. J., J. H. Kinney, J. Siebert, and F. J. Ryerson (2007), Fe-Ni-S melt permeability in olivine: Implications for planetary core formation, *Geophys. Res. Lett.*, *34*, L14306, doi:10.1029/2007GL030497.

Schulson, E. M. (1999), The structure and mechanical behavior of ice, *J. Mech.*, *51*(2), 21–27.

Shklovskii, B. I., and A. L. Efros (1984), *Electronic Properties of Doped Semiconductors*, Springer, Berlin.

Stauffer, D., and A. Aharony (1994), *Introduction to Percolation Theory*, Taylor and Francis, London.

Thomas, D. N., and G. S. Dieckmann (2003), *Sea Ice: An Introduction to Its Physics, Biology, Chemistry and Geology*, Blackwell Sci., London.

Tinga, W. R., W. A. G. Voss, and D. F. Blossey (1973), Generalized approach to multiphase dielectric mixture theory, *J. Appl. Phys.*, *44*, 3897–3902, doi:10.1063/1.1662868.

Vancoppenolle, M., C. M. Bitz, and T. Fichefet (2007), Summer landfast sea ice desalination at Point Barrow, Alaska: Modeling and observations, *J. Geophys. Res.*, *112*, C04022, doi:10.1029/2006JC003493.

Vant, M. R., R. O. Ramseier, and V. Makios (1978), The complex-dielectric constant of sea-ice at frequencies in the range 0.1–40 GHz, *J. Appl. Phys.*, *49*, 1264–1280, doi:10.1063/1.325018.

Wark, D. A., A. Williams, E. B. Watson, and J. D. Price (2003), Reassessment of pore shapes in microstructurally equilibrated rocks, with implications for permeability of the upper mantle, *J. Geophys. Res.*, *108*(B1), 2050, doi:10.1029/2001JB001575.

Weeks, W. F., and S. F. Ackley (1986), The growth, structure of sea ice, in *The Geophysics of Sea Ice*, edited by N. Untersteiner, pp. 9–164, Plenum, New York.

Wettlaufer, J. S., M. G. Worster, and H. E. Huppert (2000), Solidification of leads: Theory, experiment, and field observations, *J. Geophys. Res.*, *105*, 1123–1134, doi:10.1029/1999JC900269.

Yen, Y.-C. (1981), Review of thermal properties of snow, ice and sea ice, *Rep. 81-10*, U.S. Army Cold Region Res. and Eng. Lab., Hanover, N. H.

Zhang, S., M. S. Patterson, and S. F. Cox (1994), Porosity and permeability evolution during hot isostatic pressing of calcite aggregates, *J. Geophys. Res.*, *99*(B8), 15,741–15,760, doi:10.1029/94JB00646.

Zhu, J., A. Jabini, K. M. Golden, H. Eicken, and M. Morris (2006), A network model for fluid transport in sea ice, *Ann. Glaciol.*, *44*, 129–133, doi:10.3189/172756406781811141.

————————————

H. Eicken, J. E. Miner, and D. J. Pringle, Geophysical Institute, University of Alaska Fairbanks, 903 Koyukuk Dr., Fairbanks, AK 99775-7320, USA. (danielpringle75@gmail.com)

K. M. Golden, Department of Mathematics, University of Utah, 155 S. 1400 East, Room 233, Salt Lake City, UT 84112-0090, USA.